Supporting Information

Operando UV/Vis Spectroscopy Providing Insights into the Sulfur and Polysulfide Dissolution in Magnesium-Sulfur Batteries

Joachim Häcker*,[a], Duc Hien Nguyen[a,b], Tobias Rommel[a],

Zhirong Zhao-Karger[c], Norbert Wagner[a], K. Andreas Friedrich[a,d]

* Corresponding Author

e-mail: joachim.haecker@dlr.de

[a] Institute of Engineering Thermodynamics, German Aerospace Center (DLR), Pfaffenwaldring 38-40, 70569 Stuttgart, Germany

[b] Department of Nanochemistry, Max-Planck-Institute for Solid State Research, Heisenbergstraße 1, 70569 Stuttgart, Germany

[c] Helmholtz Institute Ulm (HIU) Electrochemical Energy Storage, Helmholtzstrasse 11, 89081 Ulm, Germany

[d] Institute of Building Energetics, Thermal Engineering and Energy Storage (IGTE), University of Stuttgart, Pfaffenwaldring 6, 70569 Stuttgart, Germany

Abstract

The magnesium-sulfur battery represents a promising post-lithium system with potentially high energy density and improved safety. However, just as all metal-sulfur systems, it is plagued with the polysulfide shuttle leading to active material loss and surface layer formation on the anode. To gain further insights, the present study aims to shed light on the dissolution characteristics of sulfur and polysulfides in glyme-based electrolytes for magnesium-sulfur batteries. Therefore, operando UV/Vis spectroscopy and imaging were applied to survey their concentration in solution and the separator coloration during galvanostatic cycling. The influence of conductive cathode additives (carbon black and titanium nitride) on the sulfur retention and cycling overpotentials were investigated. Thus, valuable insights into the system's reversibility and the benefit of additional reaction sites are gained. Based on these findings, a reduction pathway

is proposed with S_8, S_6^{2-} and S_4^{2-} being the present species in the electrolyte, while the dissolution of the long-chain S_8^{2-} and S_3^{*-} radical is unfavored. In addition, the evolution of the sulfur species concentration during an extended rest at open-circuit voltage was investigated, which revealed a three-staged self-discharge.

Supporting Information content

The Supporting Information provides details about the electrode and electrolyte preparation, as well as the optical cell and UV/Vis spectroscopy / microscopy measurement setup. In the course of establishing a reliable and stable cell setup, the influence of the anode (Mg foil vs. Mg powder pellet), electrolyte solvent (G1 vs. G4) and electrolyte volume/separator layers (1x GF, 40 µl vs. 2x GF, 65 µl) is depicted.

In the following, the calculation of the absorbance and the background selection are illustrated and an extensive table summarizing previous scientific reports of sulfur species absorbance in various solvents and electrolytes is given. Moreover, the concentration evolution during extended cycling and the reproducibility of the UV/Vis measurements are shown.

Subsequently, the properties of the applied cathode additives C45 and TiN are presented together with the SEM images and EDX analysis of the corresponding cathodes. The interesting trend of declining concentration towards the charge cut-off for the C45-cathode was reproducible, but diminishes with proceeding cycling, indicating blocking of the additional conductive reaction sites.

In the last section, the self-discharge behavior of a C45-cathode and the reproducibility of the voltage drop during 48 h OCV was investigated. A significant influence of the electrolyte could be identified, which reflects its importance for the performance and cycling stability of Mg-S batteries.

Electrode and electrolyte preparation

As basic approach, a non-infiltrated, but high-energy ball-milled sulfur-carbon composite was chosen as positive electrode material. Particularly, sulfur powder (99.5 %, Alfa Aesar) and Ketjenblack EC 600-JD (Akzo Nobel) were ball-milled in a zirconia vial with a mass ratio of 5:4 for 15 min at 500 rpm. To prevent side reactions of sulfur molecules with oxygen or water residues, the carbon powder was thoroughly dried at 100 °C under vacuum for at least 12 h and the milling vial was loaded inside an argon-filled glovebox (GS Glovebox Systemtechnik GmbH, H_2O < 1 ppm; O_2 < 1 ppm). To realize an energy-efficient (in terms of drying) and environmentally friendly (in terms of solvents) cathode preparation, a water-based slurry with carboxymethyl cellulose (CMC) and styrene-butadiene rubber (SBR) as binder system was selected. Therein, CMC offers good adhesion to the current collector and acts as dispersing agent, while SBR possesses high flexibility, strong binding force and heat resistance [1]. Therefore, deionized water and an aqueous CMC solution (3.7 wt.%, Walocel CRT 2000 PA, Dow Wolff) were pipetted to the composite and stirred over night at 400 rpm. Finally, aqueous SBR solution (40.4 wt. %, JSR TRD 102A, JSR Micro) was added to the dispersion and stirred for 3 h. After doctor blading the slurry on carbon-primed aluminum foil and drying at room temperature, a cathode comprised of 50/40/10 wt.% S/KB/CMC-SBR, with a CMC:SBR binder ratio of 1:2 results. To enhance the cathode's conductivity and provide polysulfide adsorption centers, two electrically conductive additives - C-NERGY Super C45 (Imerys Graphite & Carbon) and titanium nitride (TiN, 97 %, Chempur) - were investigated. Therefore, the same cathode preparation procedure was applied, with the S:KB ratio of 5:4 kept constant and C45 or TiN being added before the CMC solution. In this case, a cathode composition of 44.4/35.6/10/10 wt.% S/KB/additive/CMC-SBR results. All cathodes exhibit a sulfur loading of approx. 1.0 mg/cm².

For the negative electrode, magnesium pellets were fabricated from magnesium powder (99.8 %, 325 mesh, Alfa Aesar) analogous to our previous study [2]. Therefore, a 25 t manual hydraulic press (Specac), a customized stainless-steel pressing mold and ring-shaped foam templates were applied. The latter was necessary to obtain a ring-shaped anode enabling the investigation of the separator coloring. Applying 189 MPa (2 t) for one minute results in Mg pellet rings with approx. 450 µm thickness (80 mg Mg, outer and inner diameter: 14 mm and 8 mm). Anode processing was conducted inside the glovebox to avoid magnesium surface oxidation.

A fluorinated alkoxyborate, synthesized according to previous studies [3] was used as chloride-free, non-corrosive electrolyte system. The resulting magnesium salt $Mg[B(hfip)_4]_2 \cdot 3$ DME was thoroughly dried and dissolved in tetraethylene glycol dimethyl ether (G4, tetraglyme, 99 %, < 10 ppm H_2O, Acros Organics, stored over molecular sieve) to obtain a 0.2 M electrolyte.

Cell assembly

Operando investigation was enabled by the use of the optical cell ECC-Opto-Std from EL-CELL (Fig. S1). With the motivation to apply a cell setup close to practical cells, a reflection rather than transmission setup was selected. The cell assembly was carried out in an argon-filled glovebox (Jacomex, O_2 < 1 ppm, H_2O < 1 ppm) with all cell parts being dried under vacuum for 12 h at 120 °C prior to use. Furthermore, also the sulfur cathode and glass fiber separator (260 µm, Whatman GF/C) followed a vacuum drying routine of 1 h, 60 °C and 14 h, 120 °C, respectively. The cathode and separator were 6 and 10 mm in diameter, respectively. To achieve a constant background for comparable spectroscopy measurements, i.e. no cathode gleaming, a second separator layer was applied in the anode cutout. After stacking the cell parts, an electrolyte volume of 65 µL 0.2 M $Mg(B(hfip)_4)_2$ / G4 was added and the cell was closed air-tight with a sapphire window and stainless-steel cap exhibiting a 6 mm inspection window.
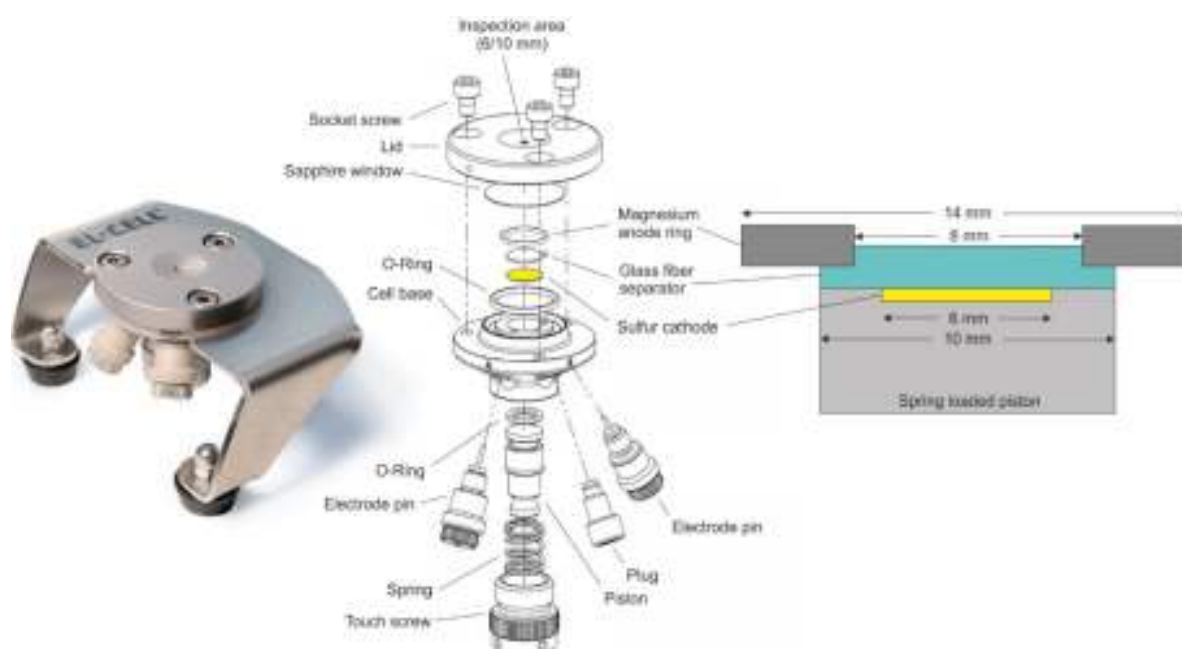

Figure S1: Cell setup for operando UV/Vis spectroscopy and microscopy applying an ECC-Opto-Std from EL-CELL with customized electrode configuration. Picture used with permission from EL-CELL GmbH. Electrode dimensions and arrangement are shown in the cross-section image.

4

Operando UV/Vis spectroscopy and imaging

Optical cells were cycled at C/20 (84 mA g^{-1}) in a voltage range of 0.05 – 3.5 V with an initial one-hour rest at open-circuit voltage (OCV) employing a BaSyTec cell test system (CTS). Despite the high charge cutoff voltage being unpractical and close to the electrochemical stability limit of the electrolyte salt [3], it was chosen to investigate the reversibility, i.e. the reoxidation of sulfur species during charge. To study the self-discharge behavior, prolonged OCV measurements with an initial 48 h OCV period are executed.

To analyze the polysulfide species and their concentration during cell operation, UV/Vis spectra were simultaneously recorded every 10 min. The UV/Vis spectroscopy setup included a light source DH-2000-Bal (Ocean Insight) that combines the continuous spectrum of a deuterium and a halogen lamp with wavelength ranges of 215–400 nm and 360–2000 nm, respectively, a spectrometer Maya2000Pro (Ocean Insight) and the corresponding software OceanView 1.6.5. Operando spectroscopy measurements were performed in reflection mode applying a reflection fiber probe (QR600-7-125BX, Ocean Insight) that consists of six illumination fibers embedding one detection fiber and a customized mounting tool to obtain reproducible measurements (Fig. S2, top left and bottom). For the background spectrum, i.e. the electrolyte-wetted separator, an apart from the missing cathode identical optical cell was assembled and measured at the same spectroscopic settings (Fig. S6).

In addition to spectroscopic measurements, operando imaging was performed to obtain a visual expression of the separator coloring and survey the electrochemical reproducibility of the optical cells. Therefore, an USB camera module (USB 2.0 UVC PC) and the software Digital Viewer were applied (Fig. S2, top right). Using a slightly larger inspection area of 10 mm in an apart from that identical cell setup, the separator coloring and anode degradation were surveyed by taking a picture every minute.
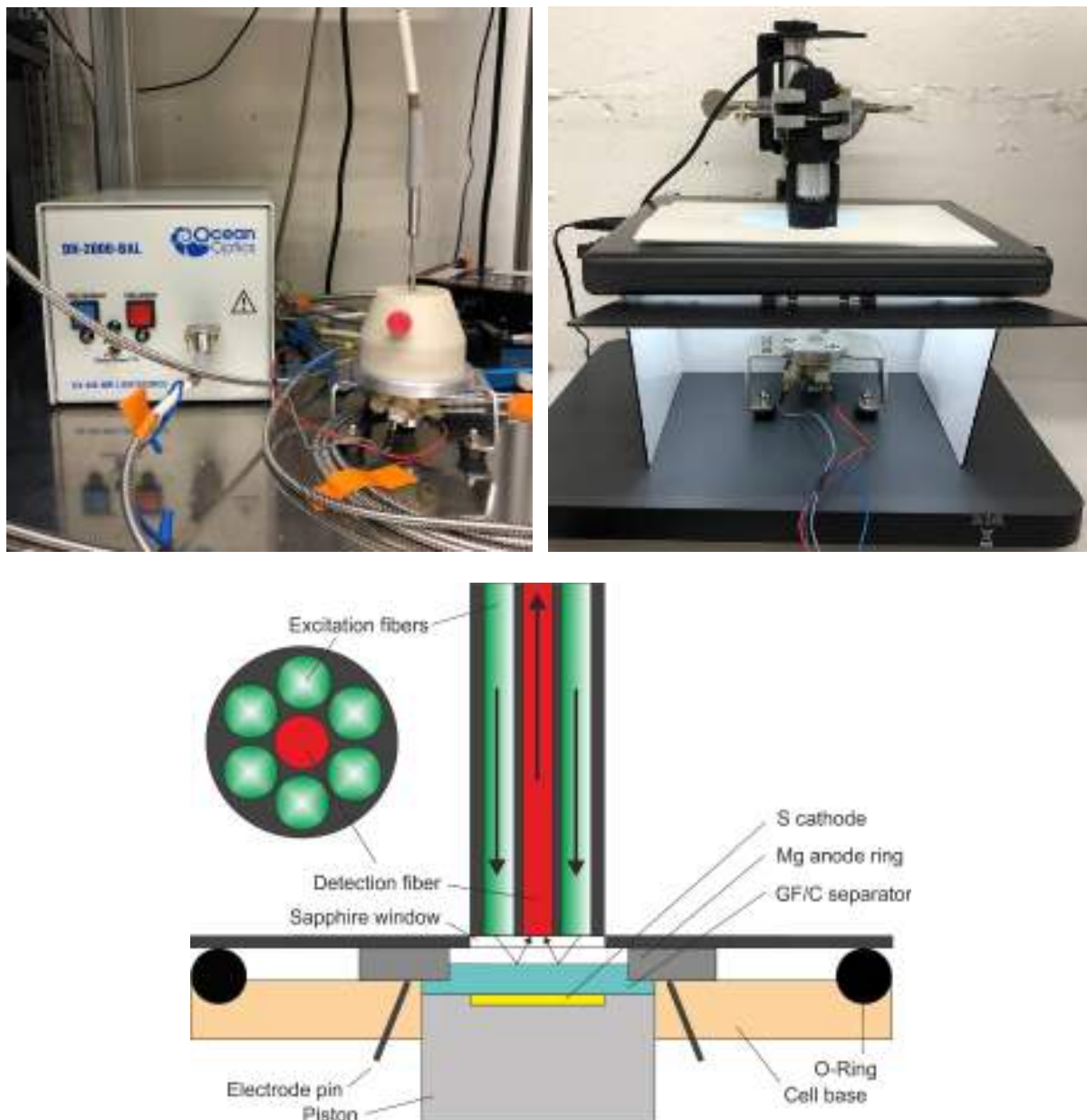
Figure S2: Top left: Setup of the operando UV/Vis spectroscopy using a customized fiber stand for reflection measurements and a light source DH-2000-Bal with Maya2000Pro spectrometer (Ocean Insight). Top right: Setup of the operando imaging with an USB camera module (USB 2.0 UVC PC). Pictures used with permission from Ocean Insight and EL-CELL GmbH. Bottom: Cross-section scheme with 6-around-1 fiber.

Selection of cell setup

To realize a reliable and reproducible cell setup, the influence of the anode, solvent and number of separator layers was investigated (Fig. S3-S5). In addition to the in-house prepared Mg powder pellet (450 μm, see electrode preparation), Mg metal foil (100 μm, Gelon) was applied as anode. In addition to tetraglyme (G4, see electrolyte preparation), ethylene glycol dimethyl ether (G1, monoglyme, 99.5 %, < 10 ppm H_2O, Acros Organics) was applied in an 0.2 M $Mg(B(hfip)_4)_2$ / G1 electrolyte. Using volatile G1 as electrolyte solvent, the cell needs to be closed before-hand and the electrolyte is added via a transfer line syringe. In this case, the electrolyte is soaked in until the separator is completely wetted, thus the volume is rather undefined.
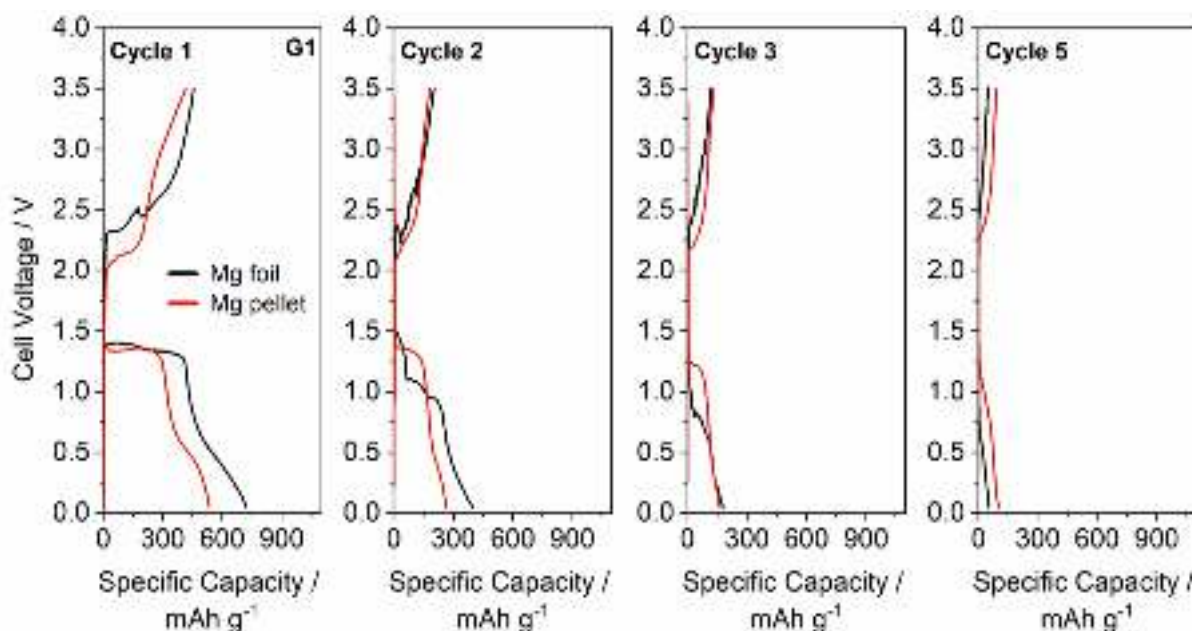

Figure S3: Influence of the anode (Mg foil or Mg pellet) on the galvanostatic cycling at C/20 applying one GF/C layer and 40 μl of an 0.2 M $Mg[B(hfip)_4]_2$ / G1 electrolyte.

Using scrapped Mg foil as anode results in unsteady charging, probably originated in formation and breakage of the SEI layer. By providing larger surface area, the Mg pellet enables stable cycling behavior – especially during charging – and was therefore chosen as anode for this study.

Regardless of the anode, both cells in Fig. S3 show fast capacity fading, which is partially assigned to the optical cell running dry as it cannot be perfectly sealed. Thus, the less volatile solvent G4 was chosen over G1 for further measurements (cf. Fig. S4).
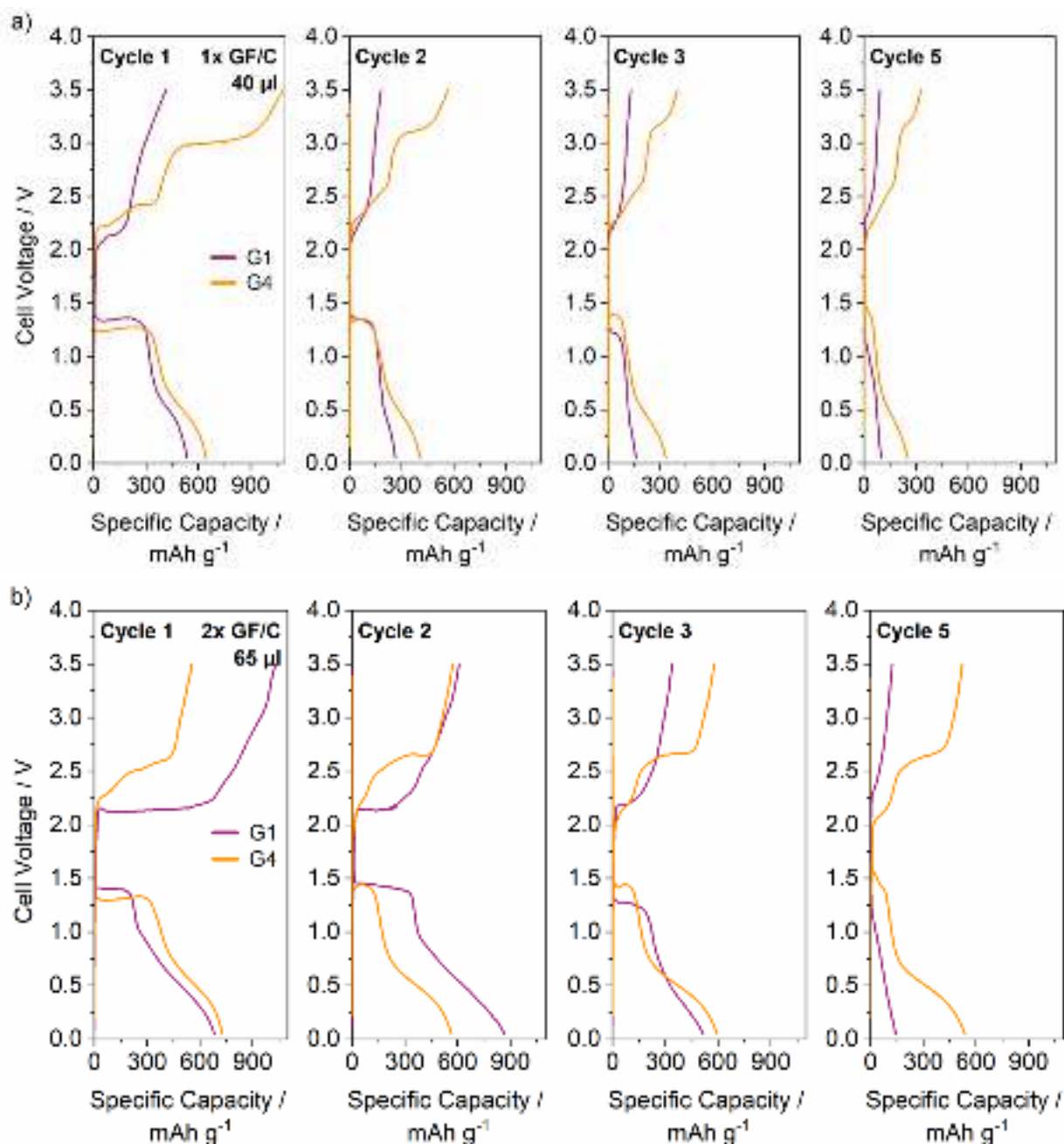
Figure S4: Influence of the electrolyte solvent (G1 or G4) on the galvanostatic cycling at C/20 applying a Mg pellet as negative electrode in an 0.2 M Mg[B(hfip)$_4$]$_2$ electrolyte with (a) 1x GF/C, 40 µl and (b) 2x GF/C, 65 µl.

As already indicated in Fig. S4, an additional GF/C separator in the anode cutout not only is necessary for the UV/Vis measurement to exclude background darkening (gleaming) by the cathode underneath, but was also found to be beneficial for stable cycling (cf. Fig. S5). This is probably mainly originated in the larger electrolyte volume (65 vs. 40 µl), which serves for better wetting and a larger fraction of reactions occurring in the liquid phase. This becomes obvious during discharge of cells with G4 (Fig.

S5b), wherein the first discharge plateau of both cells is nearly identical, whereas the second plateau is significantly shortened due to less available electrolyte. Interestingly, this affects even more the charge overpotentials with the second charge plateau not being visible in case of larger electrolyte volume. As the capacity of the second charge plateau does not provide additional capacity in the subsequent discharge (Fig. S5b, blue curve), this has to be assigned to side reactions – most probably polysulfide shuttling or electrolyte decomposition.

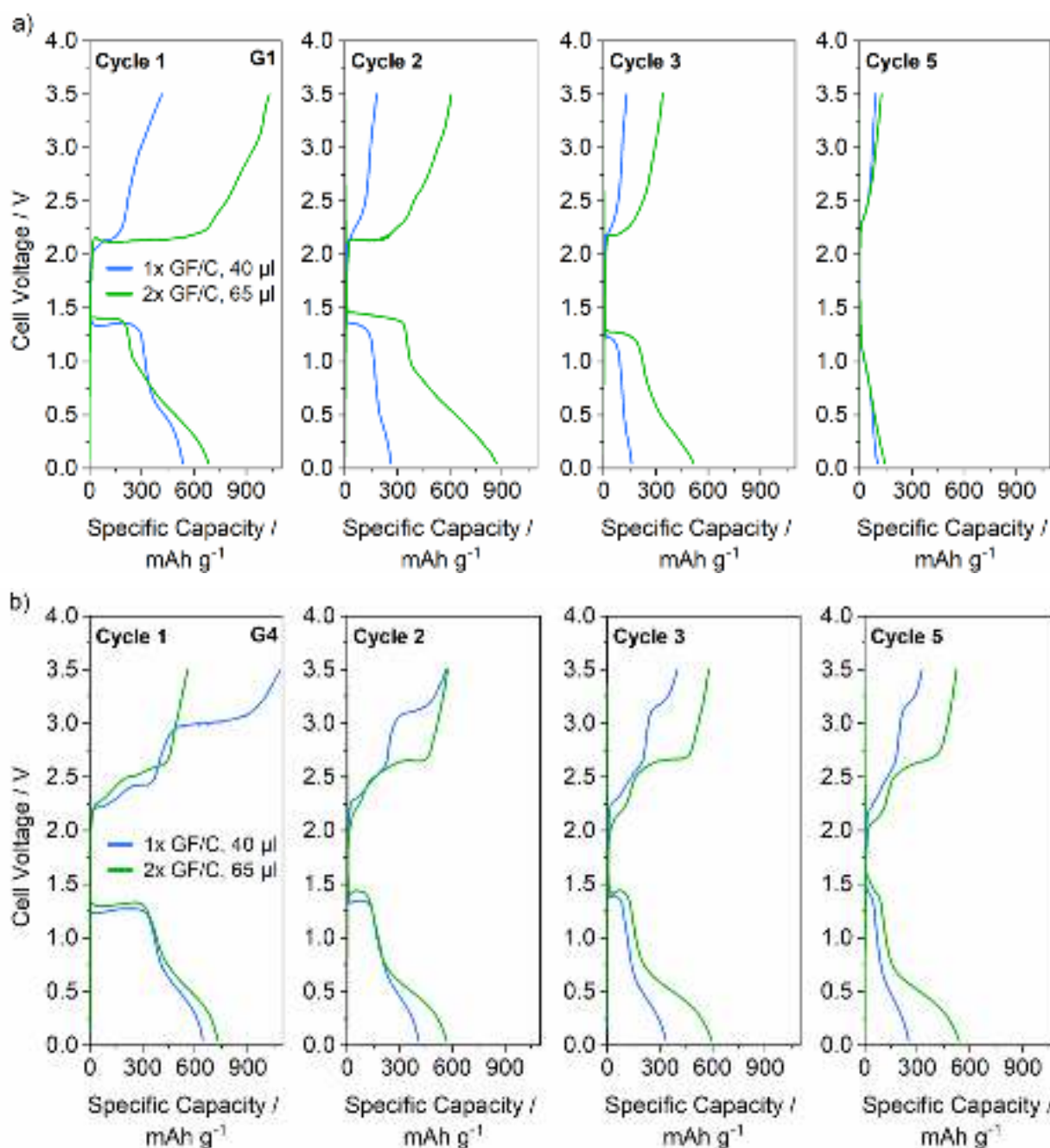Figure S5: Influence of the electrolyte volume and separator layers (1x GF/C, 40 µl and 2x GF/C, 65 µl) on the galvanostatic cycling at C/20 applying a Mg pellet as negative electrode in an 0.2 M Mg[B(hfip)$_4$]$_2$ electrolyte in (a) G1 and (b) G4.

Calculation of the absorbance

For scattering and non-luminescent samples, the sum of absorbed light fraction α, reflected light fraction R and transmitted light fraction T equals 1.

$$\propto + R + T = 1 \tag{1}$$

The absorbance A can be calculated via

$$A = -\log(1-\propto) = -\log(R + T) \tag{2}$$

and the reflectance R is defined as

$$R = \frac{I}{I_0}, \tag{3}$$

wherein I is the measured intensity at a selected wavelength and I_0 is the intensity of the background spectrum at a selected wavelength of an apart from the missing cathode identical cell. As the transmittance T can be neglected in the present case of reflectance spectroscopy, the absorbance A is calculated from the measured reflectance R of the UV/Vis spectra by:

$$A = -\log(R) = \log\left(\frac{I_0}{I}\right) = \varepsilon_\lambda \cdot c \cdot d \tag{4}$$

In the Lambert-Beer law, the absorbance A correlates with the species concentration c via the molar attenuation coefficient ε_λ (old term: molar absorptivity or extinction coefficient) and the optical path length d through the medium. In this case, the latter are unknown and a concentration calibration is difficult due to the preparation of magnesium polysulfide solutions relying on complexing ligands or an excess of reactants, which results in an undefined concentration. Therefore, a quantitative concentration analysis was abandoned and a qualitative discussion of the relative changes within one measurement are executed.

$$A_{norm} = \frac{A}{I_{768nm}} - 1 \tag{5}$$

To consider possible changes in the spectra, which are not caused by polysulfide absorbance, namely slight shifts in the lamp spectrum or drying of the separator, the absorbance A is normalized. Therefore, a wavelength region apart the polysulfide absorption is chosen (768 nm). The raw spectra (left) and the corresponding calculated absorbance with different background spectra I_0 (right) are shown in Fig. S6.
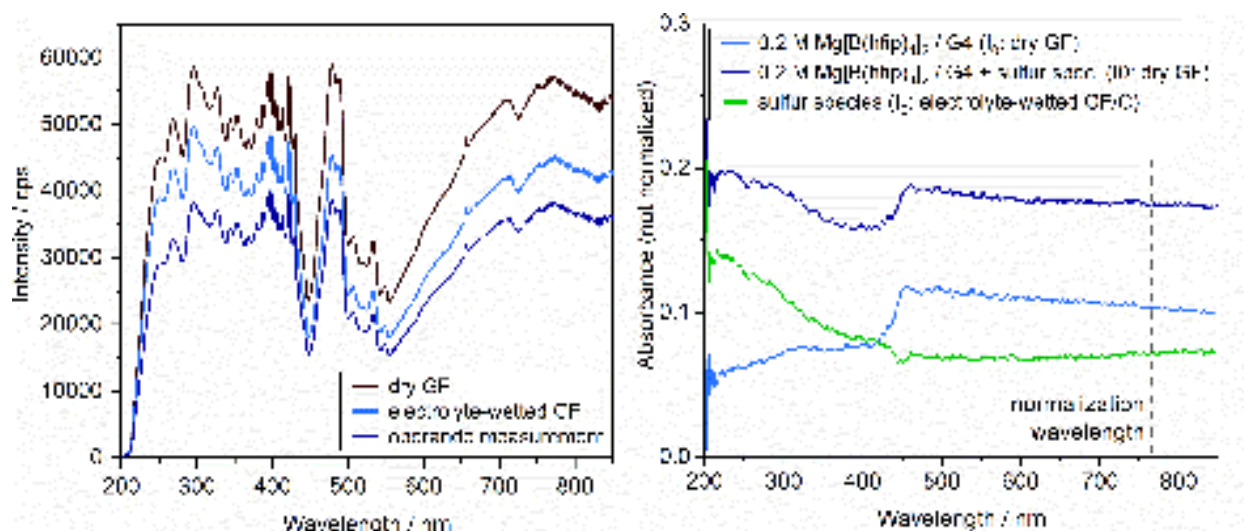
Figure S6: Left: Spectra of optical cells comprising a dry and electrolyte-wetted GF, as well as an exemplary operando spectrum (after cell assembly). Right: Corresponding absorbance of the 0.2 M Mg[B(hfip)$_4$]$_2$ / G4 electrolyte (background spectrum) and the 0.2 M Mg[B(hfip)$_4$]$_2$ / G4 electrolyte with sulfur species (after cell assembly) as well as the resulting absorbance of the sulfur species.

Table S1: Absorbance of sulfur species in various solvents and electrolytes reported in literature. The absorbance regions of the main species are summarized in Fig. 1.

	Co-Solvent	Electrolyte salt	Cation	Mode	S$_8$	S$_8^{2-}$	S$_7^{2-}$	S$_6^{2-}$	S$_5^{2-}$	S$_4^{2-}$	S$_3^{2-}$	S$_2^{2-}$	S^{2-}	S$_4^{\cdot-}$	S$_3^{\cdot-}$	Reference
G1	DOL (1:1 vol.)	1 M LiTFSI	Li$^+$	oper.		560		350/470		320/420					617	Zou 2016 [4]
	-	-	Li$^+$	ex situ	260/280					410-420					610	Bieker 2017 [5]
	-	-	Mg^{2+}	ex situ	260/280					-					660	Bieker 2017 [5]
	-	0.25 / 1.0 M MgTFSI$_2$ + 0.5 / 2.0 M MgCl2	Mg^{2+}	ex situ	200-320 (blocki-ness)					380						Ford 2021 [6]
G2	PP14-TFSI (1:1 vol.)	[(HMDS)$_2$Mg] + AlCl$_3$ + MgCl$_2$	Mg^{2+}	ex situ	250, 260			330		420						Zhao-Karger 2015 [7]
	-	0.5M MgFPB	Mg^{2+}	ex situ	200-300					approx. 420						Ford 2021 [6]
G4	-	1M LiTFSI	Li$^+$	ex situ		560, 280		470, 350, 300, 260	450	420	340	265			617	Barchasz 2012 [8]
	DOL	1M LiTFSI	Li$^+$	oper.		620* (Long-chain Li$_2$S$_x$)		550/580* (Mid-chain Li$_2$S$_x$)			450/520* (short-chain Li$_2$S$_x$)					Patel 2014 [9]
	-	1M LiPF$_6$	Li$^+$	ex situ	243, 265, 289			332		425			245, 255, 282		615	Cañas 2014 [10]
	PP14-TFSI (1:1 vol.)	[(HMDS)$_2$Mg] + AlCl$_3$ + MgCl$_2$	Mg^{2+}	ex situ	250, 260			330		420						Zhao-Karger 2015 [7]
	-	[(HMDS)$_2$Mg] + AlCl$_3$ + MgCl$_2$	Mg^{2+}	ex situ	<280nm			320-360								Yu 2016 [11]
	-	-	Li$^+$	ex situ	260/280			300-310 / 470-480		420					620	Bieker 2017 [5]
	-	-	Mg^{2+}	ex situ	260/280			300 / 480		400					640	Bieker 2017 [5]
	DOL (1:1 vol.)	0.4M Mg(TFSI)$_2$ + 0.4M MgCl$_2$	Mg^{2+}	in situ				680		520						Talian 2021 [12]

Solvent	Additive	Electrolyte	Cation	Method	S_8	S_8^{2-}	S_7^{2-}	S_6^{2-}	S_5^{2-}	S_4^{2-}	S_3^{2-}	S_2^{2-}	S^{2-}	$S_4^{\bullet-}$	$S_3^{\bullet-}$	Reference
THF	-	-	Li+	ex situ						400						Rauh 1977[13]
	-	-	Li+ Na+ K+ Cs+	in situ	265				435 (Li), 420 (Na), 445 (K), 460 (Cs)						600-625	Tobishima 1997[14]
	-	$1M\ LiEt_3BH$	Li+	in situ	240-285	480				420	385	325	240-285			Marceau 2016[15]
	-	-	Li+	ex situ	260/280					420					610	Bieker 2017[5]
	-	-	Mg2+	ex situ	260/280					370-380					650	Bieker 2017[5]
	-	-	Mg2+	ex situ	200-320 (blockiness)											Ford 2021[6]
	-	$0.35M\ MgHMDS_2 + 0.7M\ AlCl_3$	Mg2+	ex situ	200-350 (blockiness)											Ford 2021[6]
DOL	G1 (2:1 wt.)	1M LiTFSI	Li+	ex situ		237, 262, 270, 280 (Long-chain Li_2S_x)				420	334	250 (short-chain Li_2S_x)				Li 2010[16]
DMSO	-	-	n/a	ex situ		505	(618)		435						618	Bonnaterre 1972[17]
	-	-	Na+	ex situ		492		475		420					618	Martin 1973[18]
	-	-	Li+	ex situ		492		475		420	618					Rauh 1977[13]
	-	-	n/a	in situ		380, 490		320-340, 450	310-325, 420		260-270				605-624	Kim 1993[19]
	-	1M LiTFSI	Li+	oper.		492		350 / 475		325 / 420	270				617	Zou 2016[4]
	-	-	Li+	ex situ		475-490		350 / 475-490							618	Bieker 2017[5]
	-	-	Mg2+	ex situ		475-490		350 / 475-490							618	Bieker 2017[5]
DMF	-	-	n/a	ex situ		505	(618)		435						618	Bonnaterre 1972[17]
	-	0.3M TEAP	n/a	oper.	270	498									617	Gaillard 1995[20]
	-	0.25M TEAP	n/a	oper.		500									617	Levillain 1997[21]
	-	1M Li Triflate	Li+	in situ		490 (l.), 355 (c.)	470	340, 450	435	420	334	280	250	700	600	Han 2004[22]
	-	-	Li+	DFT		492 (calc.)		436 (calc.)							648 (calc.)	Kawase 2014[23]
	-	-	Li+	ex situ		500		360 / 500							620	Bieker 2017[5]
	-	-	Mg2+	ex situ		500		360 / 500							620	Bieker 2017[5]
ACN	-	$0.1M\ Et_4NClO_4$	-	in situ		350, 480		340, 450	330, 400						613	Fujinaga 1980[24]
	-	-	Li+	ex situ	270	480		360 / 480								Bieker 2017[5]
	-	-	Mg2+	ex situ	270	480		360 / 480								Bieker 2017[5]
Ionic Liquids	C4mim-DCA	1M Li Triflate	Na+	oper.				350, 460	440, 410						620	Manan 2011[25]
	Pyr14-TFSI	-	Li+	ex situ	260/280			320 / 470		420					620	Bieker 2017[5]
	Pyr14-TFSI	-	Mg2+	ex situ	260/280			320 / 470		410					630	Bieker 2017[5]
Others	EtOH	-	n/a	ex situ	250, 264, 274, 300											Heatley 1952[26]
	Ammonia	-	Li+	in situ				450	250, 330, 410				285		610	Dubois 1988[27]
	Sulfolane	1M LiTFSI	Li+	oper.		572*	567*	555*	536*	513*	494*	479*				Patel 2013[28]
	PEG-DME	$LiTFSI + LiClO_4$	Li+	oper.	280	480				420	385	325				Marceau 2016[15]
Main absor. region					250-280	475-505 560		300-360 450-500	310-330 380-440				240-285		600-660	

*wavelengths are gained from the peaks of derivative of reflectance
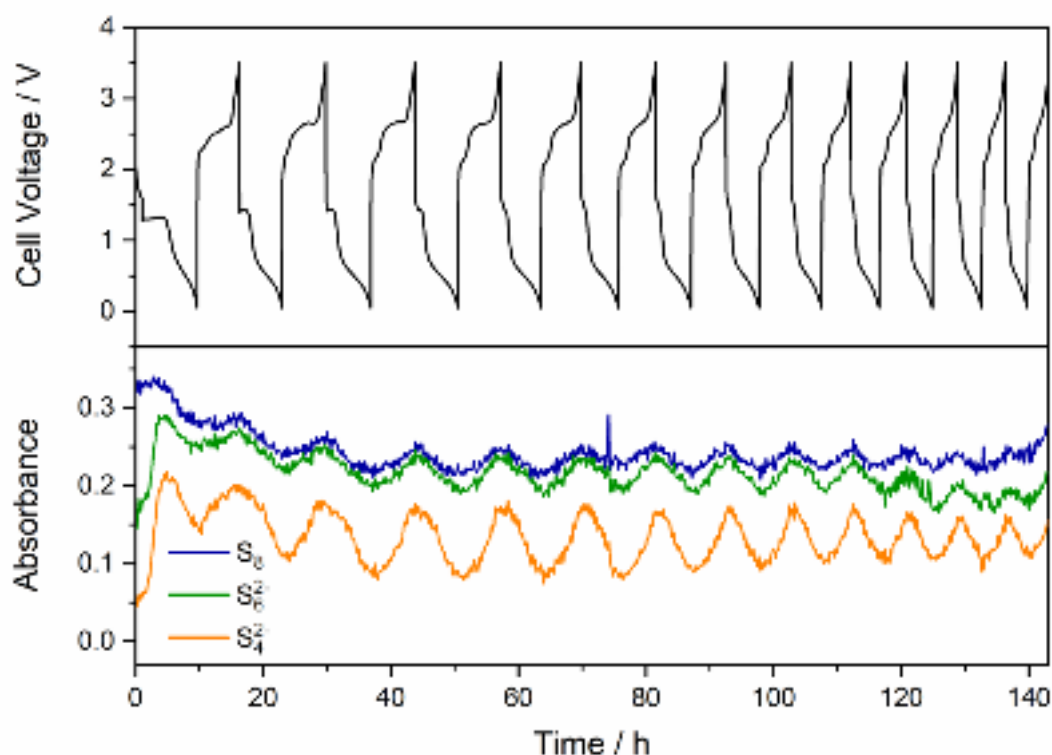
Galvanostatic cycling of cells with S/KB/CMC-SBR cathodes

Figure S7: Galvanostatic cycling at C/20 of the cell shown in Fig. 3 comprising a 0.2 M Mg[B(hfip)$_4$]$_2$ / G4 electrolyte and a S/KB/CMC-SBR (50/40/10 wt. %) cathode. An undulatory concentration trend with a constant amplitude is observed.
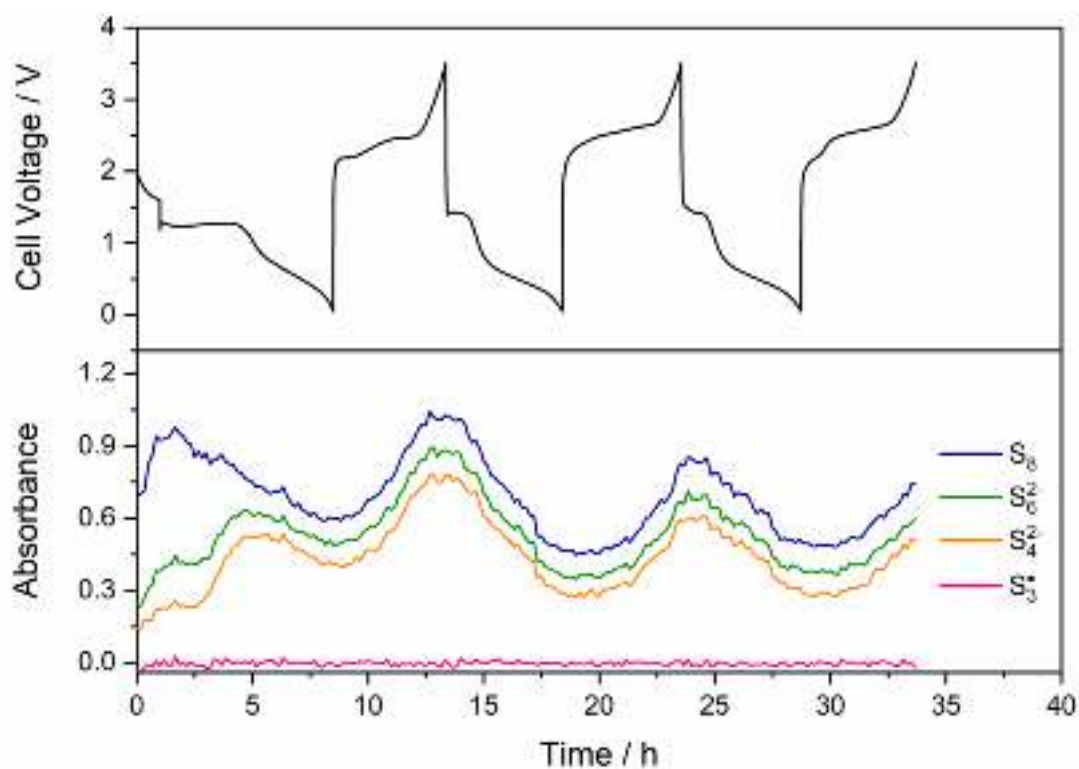

Figure S8: Voltage profile and absorbance of an operando optical cell cycled at C/20 comprising a 0.2 M Mg[B(hfip)$_4$]$_2$ / G4 electrolyte and a S/KB/CMC-SBR (50/40/10 wt. %) cathode. The qualitive trend is similar to the cell depicted in Fig.3.

13

Application of cathode additives

To provide polysulfide adsorption centers and additional reaction sites, carbon black (C45) and titanium nitride (TiN) were applied as cathode additives. Their properties are listed in Tab. S2 together with Ketjenblack.

Table S2: Properties of Ketjenblack, Super C45 and TiN. The conductivity was measured by pressing powder to a pellet (d = 1-2 mm) with 1 t for 1 min.

Compound	Supplier	Purity	Particle size / nm	Surface area / m² g⁻¹	Conductivity (pellet) / S cm⁻¹	cf. reported conductivity / S cm⁻¹
Ketjenblack EC 600-JD	Akzo Nobel	n.a.	n.a.	~1300	5.471 ± 0.163	1.5 (Vulcan XC 72)[29]
Timcal Super C45	Imerys	n.a.	n.a.	45	1.772 ± 0.069	1190 (carbon)[30]
Titanium nitride (TiN)	Chempur	97 %	20	48	0.024 ± 0.001	46 (mesoporous)[29] 42-200 (pellet)[31] 3,125 (pc thin film)[32] 4,000 (bulk)[30] 33,000 (pc thin film, CVD)[33] 20,000 – 40,000 (pc thin films, PVD)[34] 55,500 (sc thin film)[35]

The cathode morphology and additive distribution (in case of TiN) was investigated via SEM (Fig. S9-S11) applying a SE (left) and ESB detector (right). While the SE detector provides insights into the cathode microstructure, the ESB detector reflects the material contrast, which allows to distinguish between carbon, sulfur and CMC-SBR binder material. Dark areas, which might be misleadingly interpreted as molten sulfur in the SE image, can be assigned to the CMC-SBR binder by the ESB image. Sulfur, which possesses a higher ordering number (n = 16) and has to appear brighter than carbon (n = 6), is not directly visible and is therefore supposed to be covered by or incorporated in the porous carbon matrix. As the carbon areas appear brighter than the binder material, sulfur is partially contributing to the ESB signal from underneath. This is backed by the EDX analysis (Fig. S12), in which the carbon areas in all cathodes obey a large ratio of sulfur.
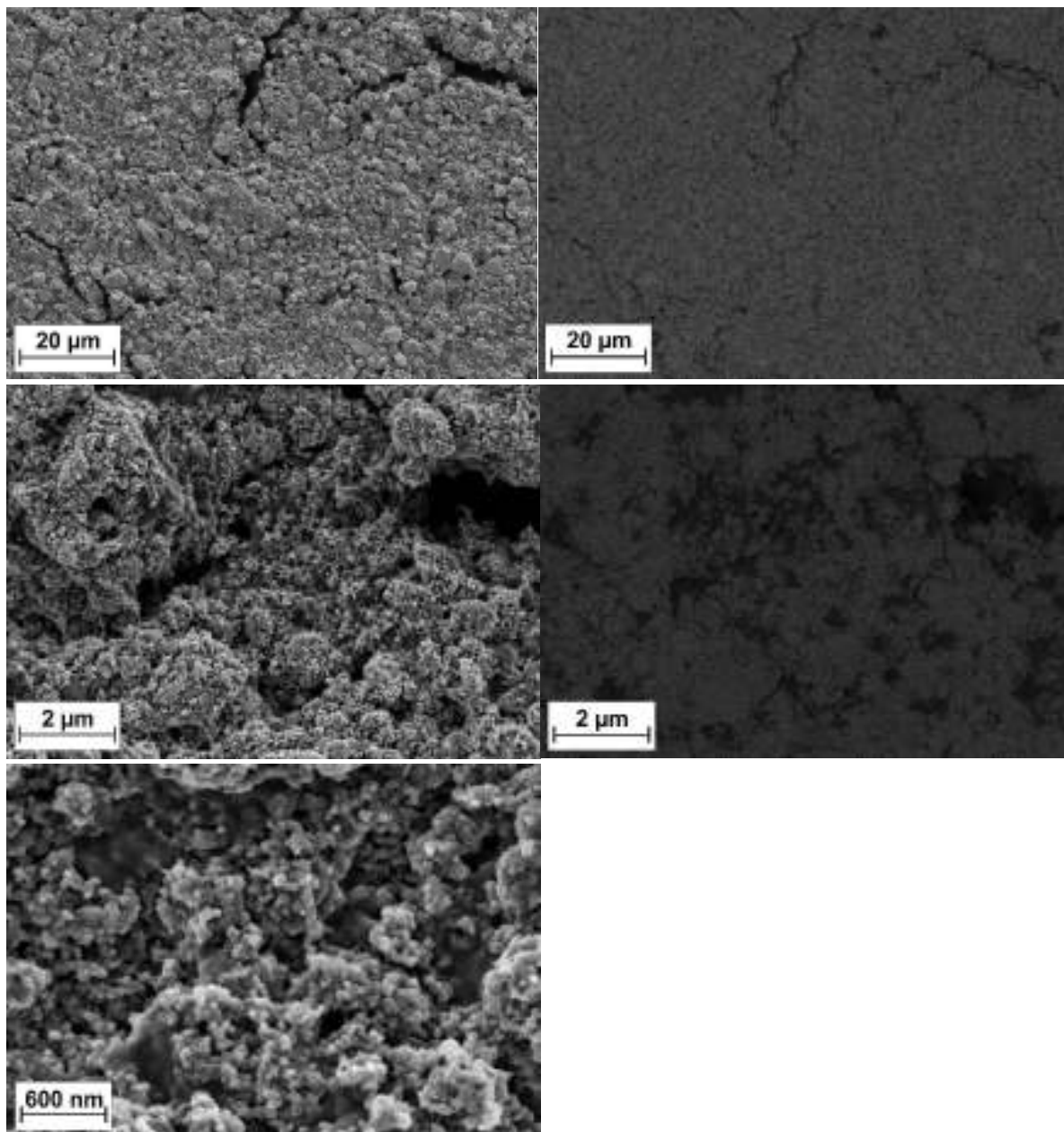
Figure S9: SEM images of the 50/40/10 wt.% S/KB/CMC-SBR cathode. Left: SE detector, right: ESB detector. Areas that have melt-like appearance in the SE image can be assigned to the CMC-SBR binder by the ESB image. Sulfur is incorporated into or at least covered by the porous carbon matrix.
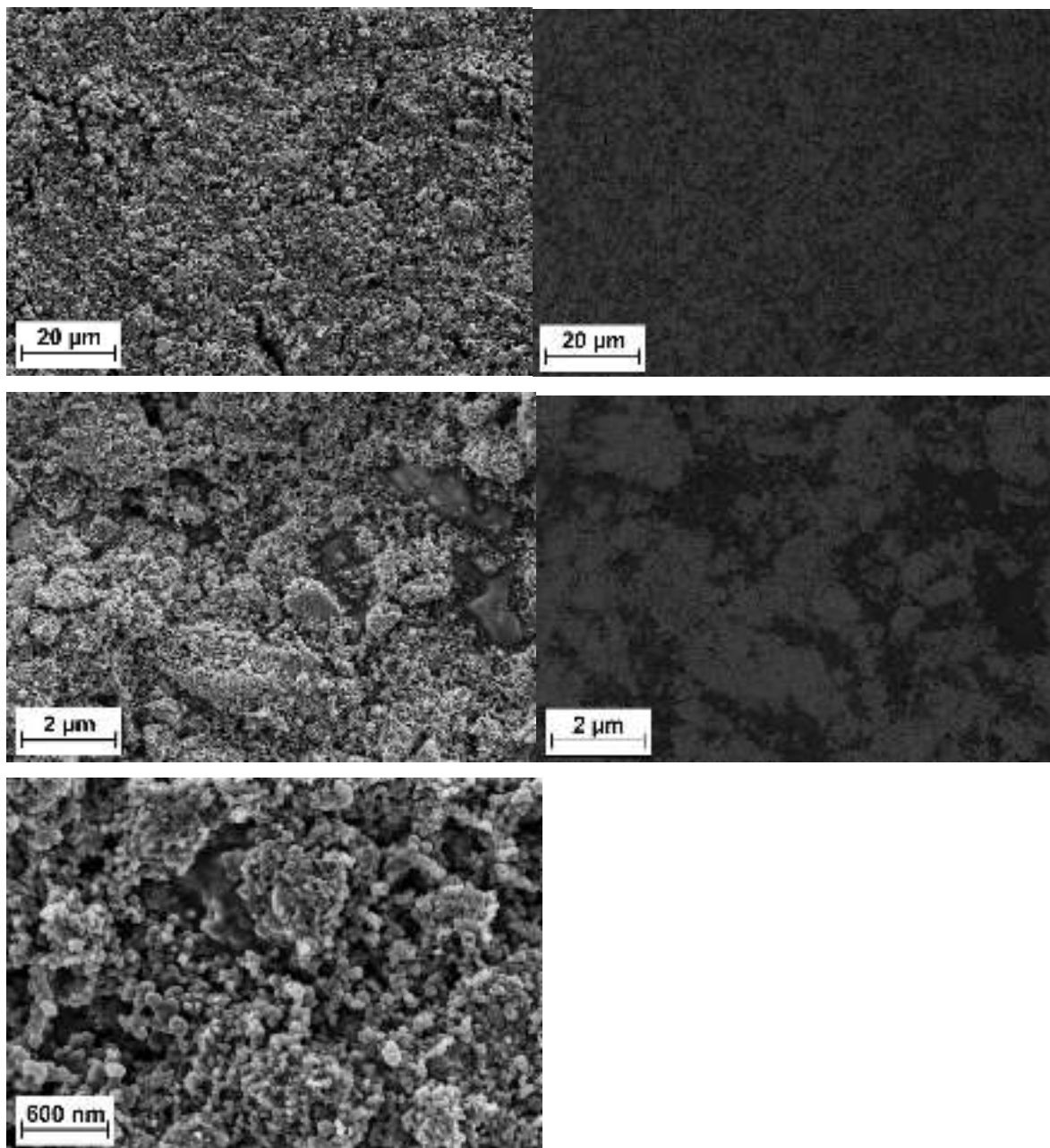
Figure S10: SEM images of the 44.4/35.6/10/10 wt.% S/KB/C45/CMC-SBR cathode. Left: SE detector, right: ESB detector. Areas that have melt-like appearance in the SE image can be assigned to the CMC-SBR binder by the ESB image. Sulfur is incorporated into or at least covered by the porous carbon matrix.
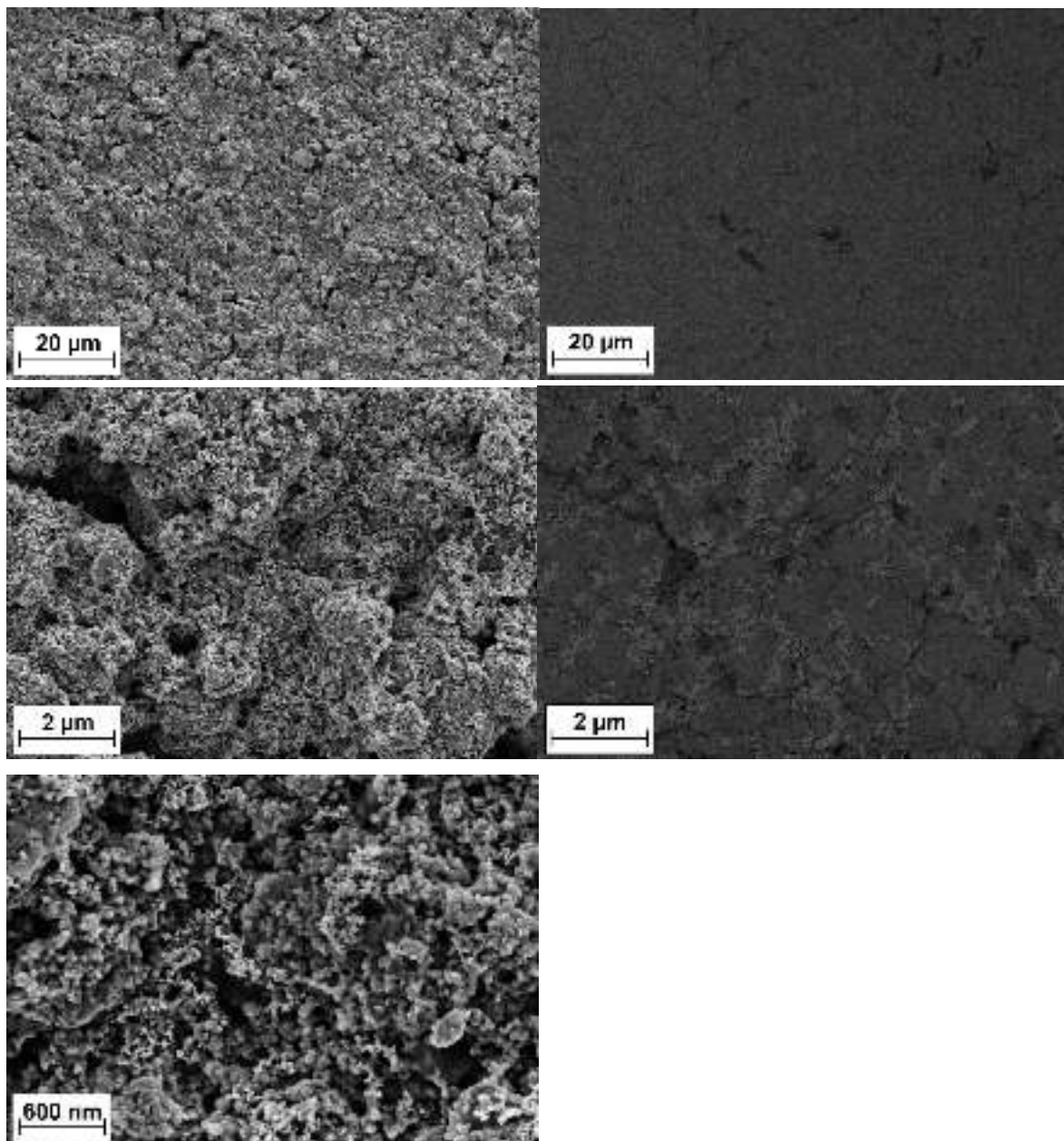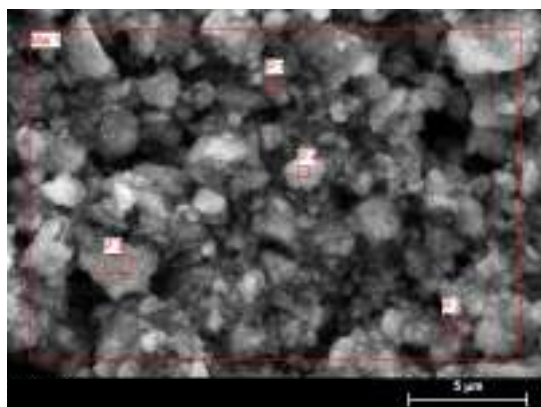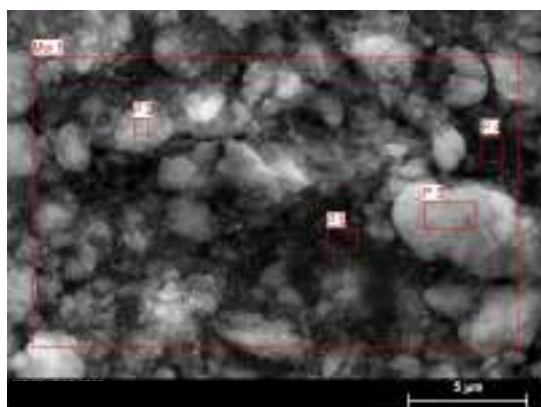
Figure S11: SEM images of the 44.4/35.6/10/10 wt.% S/KB/TiN/CMC-SBR cathode. Left: SE detector, right: ESB detector. Bright porous areas in the ESB image reflect TiN nanoparticles, which are well-dispersed.
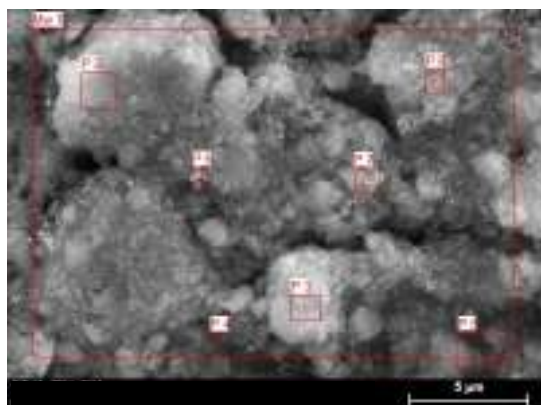
50/40/10 wt.% S/KB/CMC-SBR

Spec.(wt.%)	C	O	Na	S
Mw 1	50.24	1.22	0.52	48.03
P 1	49.34	0.85	0.44	49.37
P 2	59.88	1.39	0.39	38.34
P 3	52.75	1.19	0.40	45.66
P 4	54.33	1.10	0.50	44.07

44.4/35.6/10/10 wt.% S/KB/C45/CMC-SBR

Spec.(wt.%)	C	O	F	Na	S
Mw 1	61.12	1.51	0.92	0.46	36.01
P 2	61.85	1.89	–	0.32	35.95
P 3	54.74	1.60	–	0.22	43.44
P 4	58.81	1.37	–	0.71	39.10
P 5	75.49	0.95	6.11	–	17.45

44.4/35.6/10/10 wt.% S/KB/TiN/CMC-SBR

Spec.(wt.%)	C	N	O	Na	S	Ti
Mw 1	47.66	–	1.69	0.32	42.85	7.48
P 2	44.10	–	1.76	–	53.06	1.08
P 3	50.12	–	1.43	0.27	46.71	1.47
P 4	31.20	–	1.70	0.56	53.82	12.72
P 5	75.00	–	1.07	0.21	19.31	4.41
P 6	26.10	13.55	2.13	0.27	40.36	17.60
P 7	41.60	7.76	2.07	0.35	36.15	12.07
P 8	42.12	5.75	2.35	0.24	44.01	5.52

Figure S12: EDX analysis of the investigated cathodes. The lower than expected sulfur content arises from partial sublimation due to the high-energy electron treatment during analysis. The Na and O signal stems from the CMC binder material.

18

Table S3: Specific surface area and pore characteristics of porous materials gained from nitrogen physisorption (S/KB values refer to the carbon content). The reduced (micro-)pore volume after ball-milling of S/KB reflects partial mechanical S intrusion.

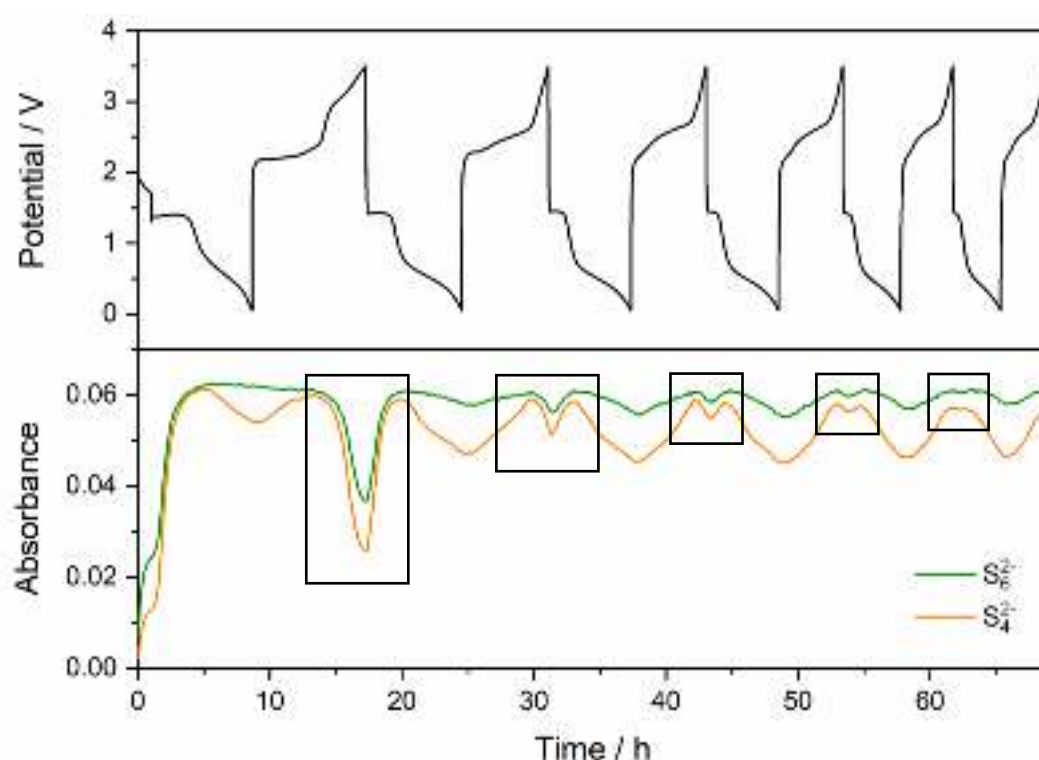| Material	Surface Area (BET) / $m^2 g^{-1}$	Pore volume (Gurvich) at 0.95 p/p^0 / $cm^3 g^{-1}$	Mesopores (BJH)		Micropores (Dubinin & Raduskevich)
			Median pore radius / nm	Min. pore radius / nm	Micropore volume / $cm^3 g^{-1}$
KB (as received)	1305.9	1.79	7.25	3.74	0.47
KB (dry milled, 500 rpm, 15 min)	1304.6	1.42	8.78	3.69	0.46
S/KB (5/4, dry milled, 500 rpm, 15 min)	151.7	0.40	20.30	3.85	0.06

Figure S13: Reproducible trend of S_4^{2-} and S_6^{2-} during cycling of a 44.4/35.6/10/10 wt.% S/KB/C45/CMC-SBR cathode (cf. Fig. 4 in manuscript). The effect of declining concentration towards the charge cut-off potential is diminished with proceeding cycling pointing to the additional conductive sites at Super C45 carbon black probably being blocked by precipitated and inactive magnesium sulfide. The unusual initial concentration decline after cell assembly in Fig. 4 was not observed in this case.

Self-discharge during 48 h OCV

The influence of the C45 cathode additive on the self-discharge behavior is shown in Fig. S14. A rather similar trend to the additive-free cathode (Fig. 8) was observed, which was expected as Super C45 does not exhibit a large pore volume for sulfur incorporation – in contrast to Ketjenblack (Tab. S3). Therefore, no beneficial sulfur retention was achieved.
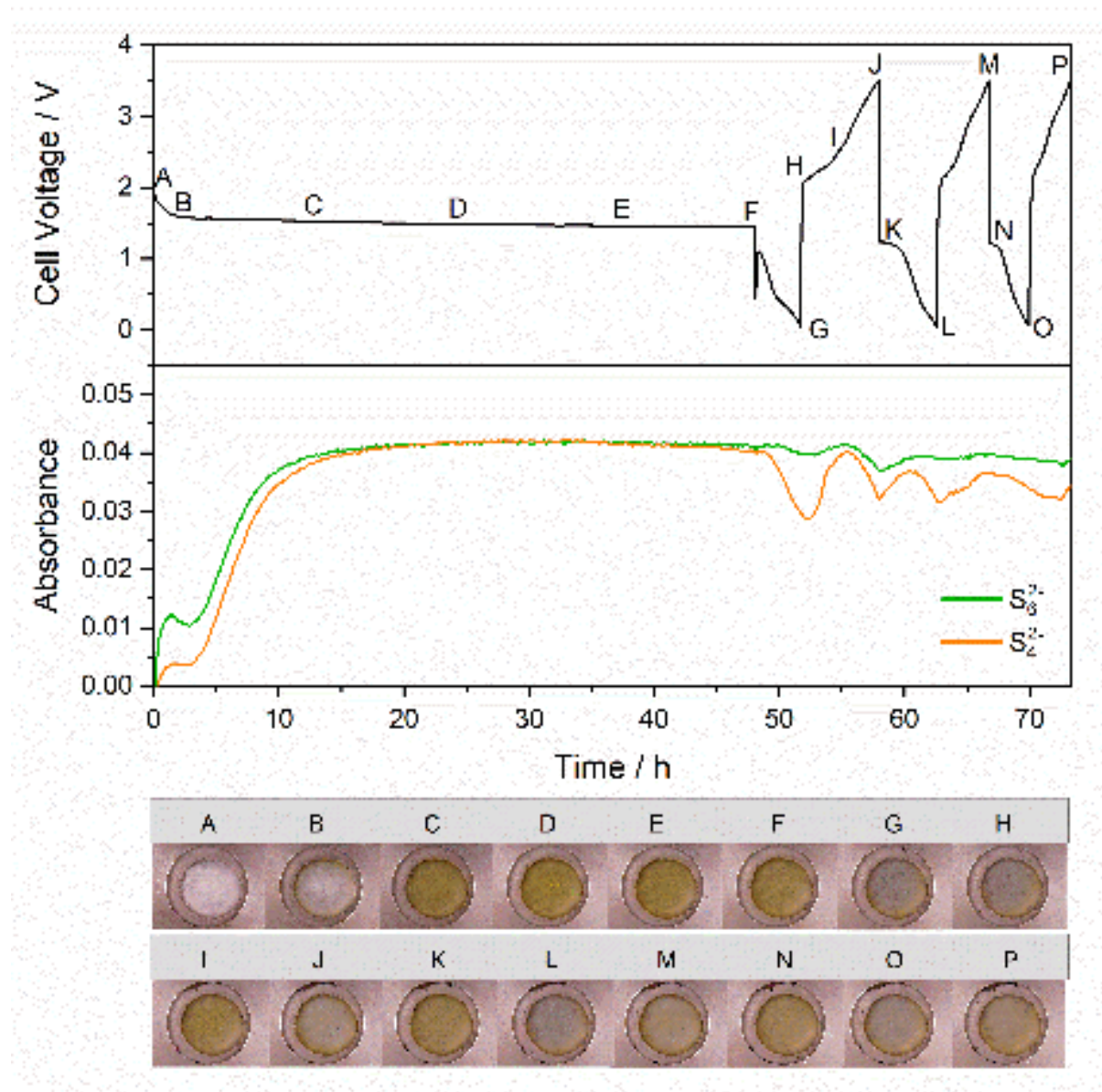

Figure S14: Voltage profile, absorbance and images of operando optical cells during 48 h OCV and subsequent cycling at C/20 comprising a 0.2 M Mg[B(hfip)$_4$]$_2$ / G4 electrolyte and a S/KB/C45/CMC-SBR (44.4/35.6/10/10 wt. %) cathode.

To confirm, that the presence of a Mg anode is necessary to initiate self-discharge an optical cell with identical setup (50/40/10 wt.% S/KB/CMC-SBR cathode with 1.0 mg/cm² sulfur loading, 2x GF/C, 65 µl 0.2 M Mg[B(hfip)$_4$]$_2$ / G4), but comprising a spacer (PE, 500 µm) instead of a Mg pellet ring is assembled and rest for two days. In contrast to the cells with a magnesium anode (Fig. 8 and S14), the separator stays uncolored, i.e. no polysulfides are generated. Thus, it can be concluded, that self-discharge only occurs by non-faradaic reduction at the Mg anode surface, while the reaction of sulfur with electrolyte species at the cathode side does not take place.

| 0 h | 12 h | 24 h | 36 h | 48 h |

Figure S15: Images of an optical cell comprising a PE spacer with same dimensions instead of a Mg powder anode. During 48 h rest, no separator coloration was observed.
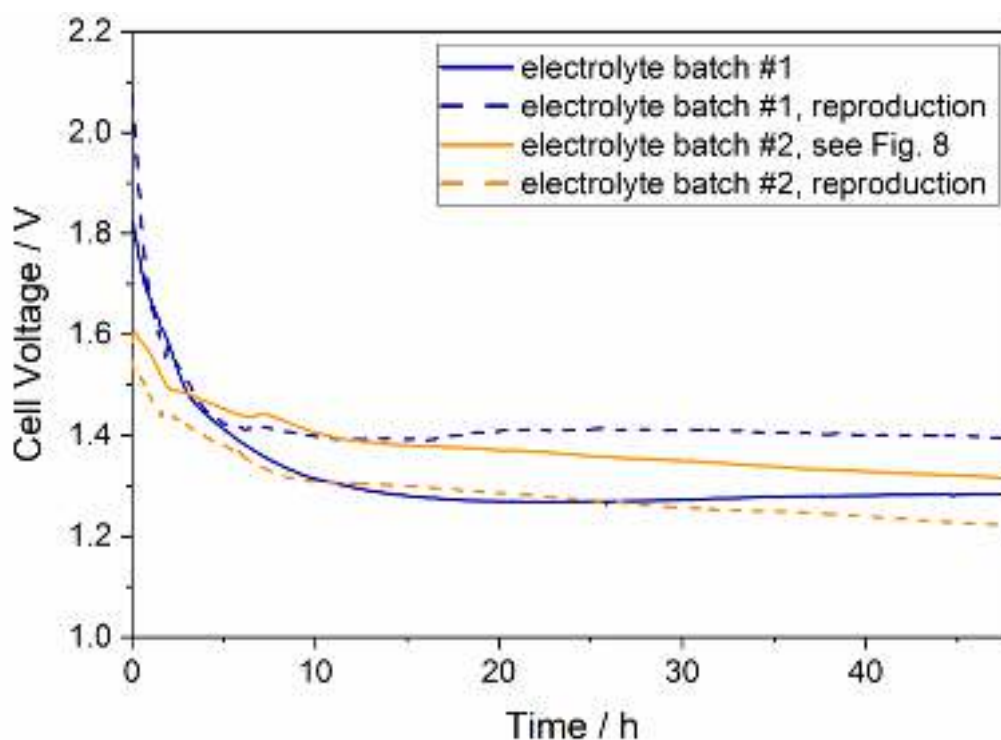

Figure S16: Cell voltage drop during 48 h OCV of four identical optical cells comprising 65 µl of 0.2 M Mg[B(hfip)$_4$]$_2$ / G4 electrolyte, a Mg powder pellet anode and a S/KB/CMC-SBR (50/40/10 wt. %) cathode with 1.0 mg/cm² sulfur loading.

To check the reproducibility of the self-discharge behavior, four optical cells with identical cell setup, namely 65 µl of 0.2 M Mg[B(hfip)$_4$]$_2$ / G4 electrolyte, Mg powder pellet

anode and S/KB/CMC-SBR (50/40/10 wt. %) cathode with 1.0 mg/cm² sulfur loading, were assembled. Their drop in cell voltage during 48 h OCV, which indicates self-discharge, is depicted in Fig. S16.

In general, differences in the initial OCV value arise from slightly differing times to connect the cell to the potentiostat after cell assembly. However, the cells significantly differ in initial potential obviously depending on the applied electrolyte batch. Despite the same electrolyte synthesis and drying procedure, slight differences in its composition and residual reactants or water impurities might be present. Despite non-current conditions, this might result in different SEI formation due to non-faradaic reaction and therefore a varied anode surface area to reduce sulfur species. In between a single electrolyte batch, the initial potential (2.0/1.8 V or 1.6/1.55V) and the overall trend (steady or slopy potential from 15-48 h) is comparable, yet a potential difference of about 0.1 V after 48 h OCV results.

This comparison demonstrates, that current Mg-S cells are a rather unstable system – not only in terms of self-discharge, but also considering reproducibility. Above all, the electrolyte seems to represents the most crucial component.

References

1.   He, M.; Yuan, L.-X.; Zhang, W.-X.; Hu, X.-L.; Huang, Y.-H., Enhanced Cyclability for Sulfur Cathode Achieved by a Water-Soluble Binder. *The Journal of Physical Chemistry C* **2011,** *115* (31), 15703-15709.

2.   Sievert, B.; Häcker, J.; Bienen, F.; Wagner, N.; Friedrich, K. A., Magnesium Sulfur Battery with a New Magnesium Powder Anode. *ECS Transactions* **2017,** *77* (11), 413.

3.   Zhao-Karger, Z.; Liu, R.; Dai, W.; Li, Z.; Diemant, T.; Vinayan, B. P.; Bonatto Minella, C.; Yu, X.; Manthiram, A.; Behm, R. J.; Ruben, M.; Fichtner, M., Toward Highly Reversible Magnesium–Sulfur Batteries with Efficient and Practical Mg[B(hfip)4]2 Electrolyte. *ACS Energy Letters* **2018,** *3* (8), 2005-2013.

4.   Zou, Q.; Lu, Y.-C., Solvent-Dictated Lithium Sulfur Redox Reactions: An Operando UV–vis Spectroscopic Study. *The Journal of Physical Chemistry Letters* **2016,** *7* (8), 1518-1525.

5.   Bieker, G.; Wellmann, J.; Kolek, M.; Jalkanen, K.; Winter, M.; Bieker, P., Influence of cations in lithium and magnesium polysulphide solutions: dependence of the solvent chemistry. *Phys. Chem. Chem. Phys.* **2017,** *19*, 11152-11162.

6.   Ford, H. O.; Doyle, E.; He, P.; Boggess, W. C.; Oliver, A. G.; Wu, T.; Sterbinsky, G. E.; Schaefer, J., Self-discharge of magnesium–sulfur batteries leads to active material loss and poor shelf life. *Energy & Environmental Science* **2021,** *14* (2), 890-899.

7.   Zhao-Karger, Z.; Zhao, X.; Wang, D.; Diemant, T.; Behm, R. J.; Fichtner, M., Performance Improvement of Magnesium Sulfur Batteries with Modified Non-Nucleophilic Electrolytes. *Adv. Energy Mater.* **2015,** *5* (3), 1401155.

8.   Barchasz, C.; Molton, F.; Duboc, C.; Leprêtre, J.-C.; Patoux, S.; Alloin, F., Lithium/Sulfur Cell Discharge Mechanism: An Original Approach for Intermediate Species Identification. *Anal. Chem.* **2012,** *84* (9), 3973-3980.

9.   Patel, M. U. M.; Dominko, R., Application of In Operando UV/Vis Spectroscopy in Lithium–Sulfur Batteries. *ChemSusChem* **2014,** *7* (8), 2167-2175.

10.   Cañas, N. A.; Fronczek, D. N.; Wagner, N.; Latz, A.; Friedrich, K. A., Experimental and Theoretical Analysis of Products and Reaction Intermediates of Lithium–Sulfur Batteries. *The Journal of Physical Chemistry C* **2014,** *118* (23), 12106-12114.

11.   Yu, X.; Manthiram, A., Performance Enhancement and Mechanistic Studies of Magnesium-Sulfur Cells with an Advanced Cathode Structure. *ACS Energy Letters* **2016,** *1* (2), 431-437.

12.   Drvarič Talian, S.; Vizintin, A.; Bitenc, J.; Aquilanti, G.; Randon-Vitanova, A.; Gaberšček, M.; Dominko, R., Magnesium Polysulfides: Synthesis, Disproportionation, and Impedance Response in Symmetrical Carbon Electrode Cells. *ChemElectroChem* **2021,** *8* (6), 1062-1069.

13.   Rauh, R. D.; Shuker, F. S.; Marston, J. M.; Brummer, S. B., Formation of lithium polysulfides in aprotic media. *Journal of Inorganic and Nuclear Chemistry* **1977,** *39* (10), 1761 - 1766.

14.   Tobishima, S.-I.; Yamamoto, H.; Matsuda, M., Study on the reduction species of sulfur by alkali metals in nonaqueous solvents. *Electrochimica Acta* **1997,** *42* (6), 1019-1029.

15.   Marceau, H.; Kim, C.-S.; Paolella, A.; Ladouceur, S.; Lagacé, M.; Chaker, M.; Vijh, A.; Guerfi, A.; Julien, C. M.; Mauger, A.; Armand, M.; Hovington, P.; Zaghib, K., In operando scanning electron microscopy and ultraviolet–visible

spectroscopy studies of lithium/sulfur cells using all solid-state polymer electrolyte. *Journal of Power Sources* **2016,** *319*, 247 - 254.

16.   Li, Y.; Zhan, H.; Liu, S.; Huang, K.; Zhou, Y., Electrochemical properties of the soluble reduction products in rechargeable Li/S battery. *Journal of Power Sources* **2010,** *195* (9), 2945-2949.

17.   Bonnaterre, R.; Cauquis, G., Spectrophotometric-Study of the Electrochemical Reduction of Sulphur in Organic Media. *Journal of the Chemical Society, Chemical Communications* **1972**, 293-294.

18.   Martin, R. P.; Doub, W. H.; Roberts, J. L.; Sawyer, D. T., Electrochemical reduction of sulfur in aprotic solvents. *Inorganic Chemistry* **1973,** *12* (8), 1921-1925.

19.   Kim, B.-S.; Park, S.-M., In Situ Spectroelectrochemical Studies on the Reduction of Sulfur in Dimethyl Sulfoxide Solutions. *Journal of The Electrochemical Society* **1993,** *140* (1), 115-122.

20.   Gaillard, F.; Levillain, E., Visible time-resolved spectroelectrochemistry: application to study of the reduction of sulfur (S8) in dimethylformamide. *Journal of Electroanalytical Chemistry* **1995,** *398*, 77-87.

21.   Levillain, E.; Gaillard, F.; Leghie, P.; Demortier, A.; Lelieur, J. P., On the understanding of the reduction of sulfur (S8) in dimethylformamide (DMF). *Journal of Electroanalytical Chemistry* **1997,** *420*, 167-177.

22.   Han, D.-H.; Kim, B.-S.; Choi, S.-J.; Jung, Y.; Kwak, J.; Park, S.-M., Time-Resolved In Situ Spectroelectrochemical Study on Reduction of Sulfur in N,N8-Dimethylformamide. *Journal of The Electrochemical Society* **2004,** *151* (9), E283-E290.

23.   Kawase, A.; Shirai, S.; Yamoto, Y.; Arakawa, R.; Takata, T., Electrochemical reactions of lithium–sulfur batteries: an analytical study using the organic conversion technique. *Phys. Chem. Chem. Phys.* **2014,** *16* (20), 9344-9350.

24.   Fujinaga, T.; Kuwamoto, T.; Okazaki, S.; Hojo, M., Electrochemical Reduction of Elemental Sulfur in Acetonitrile. *Bulletin of the Chemical Society of Japan* **1980,** *53*, 2851-2855.

25.   Manan, N. S. A.; Aldous, L.; Alias, Y.; Murray, P.; Yellowlees, L. J.; Lagunas, M. C.; Hardacre, C., Electrochemistry of Sulfur and Polysulfides in Ionic Liquids. *The Journal of Physical Chemistry B* **2011,** *115* (47), 13873-13879.

26.   Heatley, N. G.; Page, E. J., Estimation of Elemental Sulfur by Ultraviolet Absorption. *Analytical Chemistry* **1952,** *24* (11), 1854-1854.

27.   Dubois, P.; Lelieur, J. P.; Lepoutre, G., Identification and characterization of

lithium polysulfides in solution in liquid ammonia. *Inorganic Chemistry* **1988,** *27* (1), 73-80.

28. Patel, M. U. M.; Demir-Cakan, R.; Morcrette, M.; Tarascon, J.-M.; Gaberscek, M.; Dominko, R., Li-S Battery Analyzed by UV/Vis in Operando Mode. *ChemSusChem* **2013,** *6* (7), 1177-1181.

29. Cui, Z.; Zu, C.; Zhou, W.; Manthiram, A.; Goodenough, J. B., Mesoporous Titanium Nitride-Enabled Highly Stable Lithium-Sulfur Batteries. *Adv Mater* **2016,** *28* (32), 6926-31.

30. Oyama, S. T., Introduction to the chemistry of transition metal carbides and nitrides. In *The Chemistry of Transition Metal Carbides and Nitrides*, Springer: 1996; pp 1-27.

31. Choi, D.; Kumta, P. N., Nanocrystalline TiN Derived by a Two-Step Halide Approach for Electrochemical Capacitors. *Journal of The Electrochemical Society* **2006,** *153* (12), A2298-A2303.

32. Lingwal, V.; Panwar, N. S., Scanning magnetron-sputtered TiN coating as diffusion barrier for silicon devices. *Journal of Applied Physics* **2005,** *97*, 104902.

33. Kröger, R.; Eizenberg, M., Plasma induced microstructural, compositional, and resistivity changes in ultrathin chemical vapor deposited titanium nitride films. *Journal of Applied Physics* **2002,** *91* (8), 5149.

34. Bunshah, B.; Gupta, B. K., *Handbook of Tribology*. McGraw-Hill: New York, 1991.

35. Johansson, B.O.; Sundgren, J.-E.; Greene, J. E., Growth and properties of single crystal TiN films deposited by reactive magnetron sputtering. *Journal of Vacuum Science & Technology A* **1985,** *3* (2).